G. EHRET[1],✉
C. KIEMLE[1]
M. WIRTH[1]
A. AMEDIEK[1]
A. FIX[1]
S. HOUWELING[2]

Space-borne remote sensing of CO_2, CH_4, and N_2O by integrated path differential absorption lidar: a sensitivity analysis

[1] Institut für Physik der Atmosphäre, Deutsches Zentrum für Luft- und Raumfahrt (DLR) e.V., 82234 Oberpfaffenhofen, Germany
[2] National Institute for Space Research (SRON), Utrecht, The Netherlands

ABSTRACT CO_2, CH_4, and N_2O are recognised as the most important greenhouse gases, the concentrations of which increase rapidly through human activities. Space-borne integrated path differential absorption lidar allows global observations at day and night over land and water surfaces in all climates. In this study we investigate potential sources of measurement errors and compare them with the scientific requirements. Our simulations reveal that moderate-size instruments in terms of telescope aperture (0.5–1.5 m) and laser average power (0.4–4 W) potentially have a low random error of the greenhouse gas column which is 0.2% for CO_2 and 0.4% for CH_4 for soundings at 1.6 μm, 0.4% for CO_2 at 2.1 μm, 0.6% for CH_4 at 2.3 μm, and 0.3% for N_2O at 3.9 μm. Coherent detection instruments are generally limited by speckle noise, while direct detection instruments suffer from high detector noise using current technology. The wavelength selection in the vicinity of the absorption line is critical as it controls the height region of highest sensitivity, the temperature cross-sensitivity, and the demands on frequency stability. For CO_2, an error budget of 0.08% is derived from our analysis of the sources of systematic errors. Among them, the frequency stability of ± 0.3 MHz for the laser transmitter and spectral purity of 99.9% in conjunction with a narrow-band spectral filter of 1 GHz (FWHM) are identified to be challenging instrument requirements for a direct detection CO_2 system operating at 1.6 μm.

PACS 42.68.Wt; 95.75.Qr

1 Introduction

Long-lived atmospheric species such as carbon dioxide (CO_2), methane (CH_4), and nitrous oxide (N_2O) have been recognised by the International Panel of Climate Change as the most important greenhouse gases, the concentrations of which increase rapidly due to human activities since the industrial revolution [1]. In order to better predict the behaviour of the climate system and to help constrain political conventions on greenhouse gas avoidance, a more accurate knowledge of the sources and sinks of these gases in terms

✉ Fax: +49-8153-28-1271, E-mail: gerhard.ehret@dlr.de

of location, magnitude, and variability on a global basis is essential.

Greenhouse gas fluxes at the Earth's surface exhibit a complex pattern in space and time and cannot be directly measured by satellite observations. Concentration measurements of the vertical total column may be used to infer surface sources and sinks by means of inverse models that describe atmospheric transport and mixing [2]. Initial estimates reveal that the required level of measurement accuracy is exceptionally high and cannot be provided by the current global observing system [2, 3]. The main drawback of passive sounders in the infrared spectral region is related to their atmospheric weighting functions which favour the middle and the upper troposphere (e.g. 5 km and above) rather than the lower troposphere where the sources and sinks reside [4, 5]. In the solar backscatter region major limitations arise due to atmospheric aerosol interference [6] and from the fact that these systems lack sensitivity at high latitudes due to the unfavourable Sun angle [7, 8].

High measurement sensitivity is expected from making use of integrated path differential absorption (IPDA) lidar, where the strong lidar echoes from cloud tops or the Earth's surface can be used to infer the trace gas column from soundings at two frequencies in the vicinity of an absorption line [9]. The possibility for minimising potential sources of systematic errors which may arise from unknown temperature profiles, water vapour interference, and aerosols is a further advantage of this measurement technique. In addition, sounding in the wing of an absorption line would enable high sensitivity in the low troposphere.

There are a few publications reporting successful measurements of atmospheric CO_2 columns by ground-based instruments using laser transmitters at wavelengths near 2.0 μm and 4.8 μm [10–13]. In the case of active remote sensing of CH_4 there are several operational instruments for gas leak detection operating in the 3.3-μm or 1.6-μm spectral regions [14–17]. Various laser transmitters are employed such as optical parametric oscillators (OPOs), $CO:MgF_2$ lasers, DF lasers, Ti:sapphire lasers with Raman shifting, or harmonic generation of CO_2 lasers [18]. Differential absorption lidar (DIAL) measurements of range-resolved CO_2 profiles using a pulsed single-frequency Tm:Ho:YLF laser at 2.05-μm wavelength in combination with heterodyne detec-

tion principles are reported in [19]. Only two active remote sensing systems for the detection of N_2O have been developed yet [20, 21]. Both systems use the topographic target return of a pulsed chemical laser (DF) at 3.9 µm.

Space-borne lidar systems have been the subject of extensive investigations since the mid 1970s resulting in mission and instrument concepts mainly for the measurement of meteorological parameters such as aerosols and clouds [22–24], wind [25], and water vapour profiles [26], as well as surface elevation [27]. Although the feasibility of active remote sensing of CO_2 from space has already been suggested in [28] there is still enormous lack of knowledge of the required performance on the instrument level. To close this gap, observational requirements for the measurement of sources and sinks of the most important greenhouse gases CO_2, CH_4, and N_2O were recently derived in a comprehensive requirements definition study [29]. Forward model simulations were used to calculate the temporal and spatial variabilities of the trace gases while inverse calculations have been carried out to model the reduction in surface flux uncertainty through measurements performed by a hypothetical IPDA lidar instrument embarked on a space-borne platform. As a result, for an adequate quantification of the relevant processes controlling sources and sinks of the greenhouse gases, the precision for the relative random error should range between 0.26% and 1.3% for CO_2, between 0.4% and 2% for CH_4, and between 0.06% and 0.3% for N_2O for the column integrated dry air mixing ratio. The error boundaries represent target and threshold observational requirements for a spatial cell of 50–500 km. The observational requirements for the systematic error are expected to be even more stringent and range between 0.02% and 0.26% for CO_2 in order to resolve regional gradients such as the North–South gradient in the CO_2 distribution or disturbances in the seasonal cycle.

In the study in hand we investigate the measurement performance of different classes of IPDA lidar instruments and compare to the above observational requirements. In Sect. 2 the methodology is introduced. Section 3 reports the random error and sensor optimisation with the aim to meet the stringent target observational requirements. In Sect. 4 sources of systematic errors are discussed and an error budget is presented for a CO_2 system operating at 1.6 µm. Section 5 discusses critical instrument sub-systems and implications for a possible instrument realisation. Section 6 summarises the most important findings of this study.

2   Methodology

2.1   *IPDA lidar principle*

The performance model used in this study assumes a space-borne DIAL instrument which measures light scattered and reflected from ground surfaces in the nadir viewing direction along the satellite flight track. We restrict our analysis to the simplest case of only two sounding frequencies, in the following denoted as on-line and off-line. Due to gas absorption along the measurement path, sounding at on-line results in a significantly larger atmospheric extinction compared to off-line which serves as a reference. Hence, the columnar averaged dry air mixing ratio of the greenhouse gas can be directly inferred from comparison of the two lidar signals using

the following expression for the measured differential optical depth:

$$
\begin{aligned}
\delta_{gas}(r_G) &\equiv \int_{r_{TOA}}^{r_G} q_{gas}(r') \left(1 - q_{H_2O}(r')\right) \\
&\quad \times n_{air}(r') \left(\sigma_{on}(r') - \sigma_{off}(r')\right) dr' \\
&= \frac{1}{2} \ln \frac{P_{off}(r_G)}{P_{on}(r_G)} + C,
\end{aligned} \tag{1}
$$

with

$$
\begin{aligned}
C = \frac{1}{2} \Bigg[&\ln \frac{D_{on}(\nu_{on})}{D_{off}(\nu_{off})} + \ln \frac{O_{on}(r_G)}{O_{off}(r_G)} + \ln \frac{E_{on}}{E_{off}} + \ln \frac{\varrho_{on}(r_G)}{\varrho_{off}(r_G)} \\
&- 2(\delta_A(\nu_{on}, r_G) - \delta_A(\nu_{off}, r_G)) \Bigg].
\end{aligned}
$$

In this equation q_{gas} is the dry air volume mixing ratio of the greenhouse gas, n_{air} is the air number density, q_{H_2O} is the volume mixing ratio of water vapour, and $\sigma_{on} - \sigma_{off}$ is the differential absorption cross section. The integration runs from the top of the atmosphere r_{TOA} down to the Earth's surface r_G. Equation (1) results from application of the simplified hard target lidar equation [30] expressed by

$$
P_{on,off}(r_G) = D_{on,off} \frac{A}{r_G^2} O_{on,off} \varrho_{on,off}^* \tau_{on,off}^2 \frac{E_{on,off}}{\Delta t_{eff}}, \tag{2}
$$

where $P_{on,off}$ are the radiation fluxes entering the detector area from soundings at both wavelengths, D is the total optical efficiency of the transmitter/receiver system, O is the overlap function between the light beam and the field of view of the receiving telescope, E is the pulse energy of the transmitted laser radiation, Δt_{eff} is introduced to account for the effective pulse length of the lidar returns, τ is the one-way atmospheric transmission, and ϱ^* [sr^{-1}] is the target parameter defined as the reflected power per steradian towards the receiver divided by the incident power [31]. For an ideal Lambertian surface the latter is commonly expressed by ϱ/π, where ϱ is called the reflectivity of the target. The parameter δ_A of (1) represents the optical depth of all other constituents of the atmosphere interacting with the laser radiation such as aerosols, air molecules, and other trace gases.

A key role in (2) is played by Δt_{eff}, which accounts for the spread of the reflected laser pulses in the time domain. In general, this parameter is a function of the laser pulse length $\Delta\tau_L$, the detector impulse response time $\Delta\tau_D \approx 1/(3B)$, and the time spread $\Delta\tau_T$ caused by a structured surface. If we assume Gaussian distributions for these broadening effects, the effective pulse length in the time domain can be derived from the convolution theorem, where the spread is given by the geometrical sum of the individual half-widths according to

$$
\Delta t_{eff} = \sqrt{\Delta\tau_L^2 + \left(\frac{1}{3B}\right)^2 + \left(\frac{2\Delta h}{c}\right)^2}, \tag{3}
$$

where B is the electrical bandwidth of the detector/amplifier system, Δh is the effective target altitude within the footprint of the laser pulse (e.g. given by the slope of the surface with respect to normal incidence), and c is the speed of light.

It is worth mentioning that (1) is based on several simplifications. In particular, lidar echoes caused by inelastic interaction processes such as Raman scattering or fluorescence from topographic targets are assumed to be negligible or being removed with an appropriate narrow-band optical filter in the receiver channels. Furthermore, a possible Doppler-shifted absorption line originating from pointing off-nadir and a limited spectral bandwidth (e.g. spectral profile) of the emitted laser pulses are not considered. Consequences of deviations from the latter simplification are discussed in Sect. 4.

2.2 *Weighting function*

Despite the fact that the IPDA lidar method does not provide range-resolved measurements, some information on the vertical distribution of the greenhouse gases can be obtained from examination of the vertically weighted column volume mixing ratio $\bar{q}_{gas}$ introduced in [32]:

$$\bar{q}_{gas} = \frac{\int_{p_{TOA}}^{p_{surf}} q_{gas}(p) w(p,T)\,dp}{\int_{p_{TOA}}^{p_{surf}} w(p,T)\,dp}\,. \qquad (4)$$

In this equation a weighting function w appears, which can be explicitly expressed with the notation of (1) by $w(p,T) = n_{air}(p,T)(\sigma_{on}(p,T) - \sigma_{off}(p,T))(-\partial r/\partial p)$, with n_{air} and σ commonly given in pressure and temperature coordinates. For simplicity we refer to dry air only. The weighting function in principle describes the relative contribution of an atmospheric layer to the total column of the trace gas volume mixing ratio at pressure p and temperature T. The integration in (4) runs from the pressure at the top of the atmosphere p_{TOA} down to the surface pressure p_{surf}. Using the hydrostatic equation and the ideal gas law, the transformation from altitude to pressure coordinates can be written by $\partial r/\partial p = -k_B T/(p M_{air} g)$ with k_B being Boltzmann's constant and g the normal gravity; hence, w simplifies to

$$w(p,T) = \frac{\sigma_{on}(p,T) - \sigma_{off}(p,T)}{g M_{air}}\,, \qquad (5)$$

where M_{air} denotes the average mass of a dry air molecule. Equation (5) indicates that selection of the laser frequency for the molecular absorption cross sections can have a strong influence on the shape of the weighting function as illustrated in Figs. 1 and 2. In Fig. 1 three typical weighting functions normalised to unity associated with soundings in the line centre as well as at line wing positions with a frequency displacement from the line centre of γ_L and $2\gamma_L$ are shown, with γ_L denoting the collisional half-width of line 'a' from Table 1. For
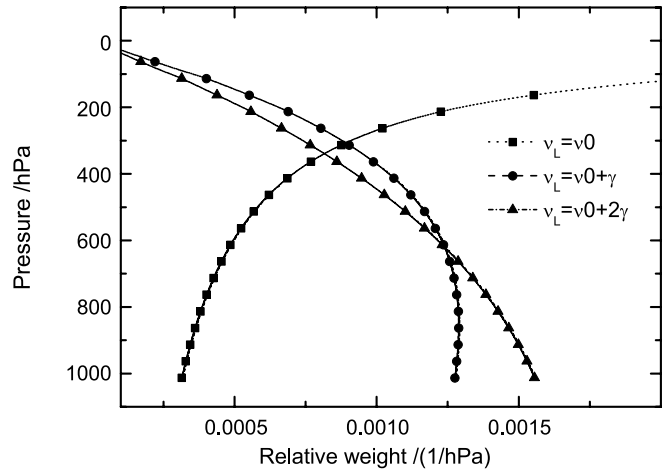

FIGURE 1 Relative weight of the greenhouse gas column content at different pressure levels for three different laser frequency positions ν_L in the vicinity of a trace gas absorption line with the centre frequency ν_0 as indicated in Fig. 2
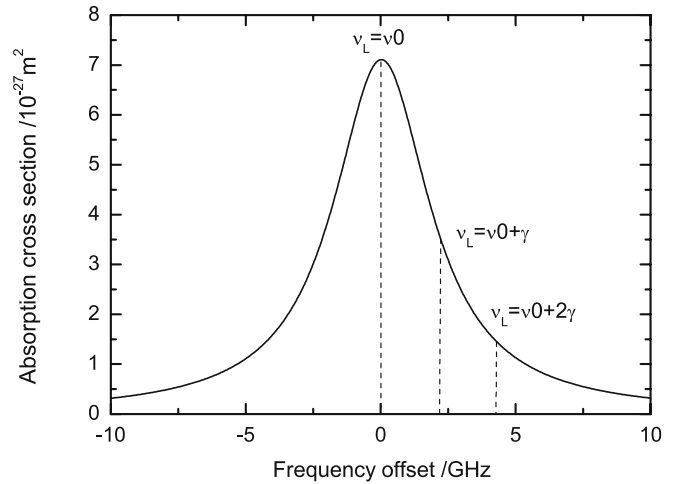

FIGURE 2 Molecular absorption cross section of line 'a' from Table 1 as function of frequency detuning from centre line $\nu_0 = 0$ for $T = 288$ K and $p = 1013$ hPa. The *dashed lines* indicate the laser frequency displacement in units of the collisional half-width γ_L from the centre line

the calculations of the absorption cross sections a monochromatic laser line profile was assumed and the molecular line shape has been modelled by a Voigt profile approximation (see Sect. 3.4). It follows that measurements of greenhouse gases at the line centre would have their maximum sensitivity in the upper troposphere and stratosphere, while soundings at frequency displacements $\Delta\nu = 2\gamma_L$ off the line centre would yield a high sensitivity in the low troposphere. For a more

Species	Wavelength µm	Optimum on-line cm^{-1}	Line centre cm^{-1}	S_0 cm^2 cm^{-1}	E'' cm^{-1}	Line label	See Fig.
CO$_2$	1.6	6361.2219	6361.2509	1.82×10^{-23}	133.00	a	3a
		6212.8203	6212.7953	1.60×10^{-23}	133.44	b	
	2.1	4875.6275	4875.7487	1.74×10^{-22}	362.79	c	3b
		4833.9070	4833.7700	2.25×10^{-22}	234.08	d	
CH$_4$	1.6	6057.1224	6057.0861	1.28×10^{-21}	104.77	e	3c
N$_2$O	3.9	2542.3427	2542.3536	1.80×10^{-20}	231.24	f	3d

TABLE 1 Overview of optimised on-line positions (vacuum wave numbers) from [29] and absorption line parameters from the HITRAN'96 database [37]

uniform sensitivity over the whole troposphere a frequency displacement around γ_L seems appropriate. About 18% for $\Delta \nu = 2\gamma_L$, 15% for $\Delta \nu = \gamma_L$, and 4% for $\Delta \nu = \nu_0$ of the total optical depths can be attributed to greenhouse gas absorption within the first km above ground. It is worth mentioning that a frequency displacement $> 2\gamma$ would not lead to a remarkably better sensitivity in the first km near the ground, because w becomes saturated ($\sim 19\%$ of the total optical thickness). This is because of the shape of the molecular absorption cross section approaching a Lorentz-type profile giving the relation $w \sim p$.

3 Random error

3.1 *Performance model*

The measurement sensitivity of the optical depth expressed by (1) was analysed in terms of the mean signal-to-noise ratio (SNR) of the lidar returns given by $\mathrm{SNR}_{\mathrm{on,off}} \equiv \sqrt{\langle P_{\mathrm{on,off}}\rangle^2/\langle \Delta P^2_{\mathrm{on,off}}\rangle}$. Provided that the laser pulse energy measurement may additionally be affected by statistical fluctuations where the signal-to-noise ratio is given by $\mathrm{SNR}^L_{\mathrm{on,off}} \equiv \sqrt{\langle (E^L_{\mathrm{on,off}})\rangle^2/\langle (\Delta E^L_{\mathrm{on,off}})^2\rangle}$, the random error of the optical depth was estimated from first order error propagation expressed by

$$\left\langle \Delta\delta^2_{\mathrm{gas}}\right\rangle = \frac{1}{4}\left(\frac{1}{\mathrm{SNR}^2_{\mathrm{on}}} + \frac{1}{\mathrm{SNR}^2_{\mathrm{off}}} + \frac{1}{\left(\mathrm{SNR}^L_{\mathrm{on}}\right)^2}\right.$$
$$\left. + \frac{1}{\left(\mathrm{SNR}^L_{\mathrm{off}}\right)^2}\right)\frac{1}{n_{\mathrm{shots}}}, \tag{6}$$

where n_{shots} denotes the number of statistically independent pulse pairs. The main contribution to the random error arises from signal fluctuations of the lidar measurements due to speckle noise as well as detection noise, both influencing the overall $\mathrm{SNR}_{\mathrm{on,off}}$. The impacts of these noise sources on the measurement sensitivity are quite different and critically dependent on the type of detection method used as shown in the following paragraphs.

3.2 *The direct detection instrument*

A direct detection instrument converts the incoming photon flux entering the detector's surface to a measurable signal current through the generation of a suitable amount of charge carriers by means of internal and external amplification processes. The mean CNR (carrier-to-noise ratio) for each wavelength can be calculated using [33]:

$$\mathrm{CNR} = \frac{PMR}{\sqrt{\langle \Delta I^2_N\rangle}}, \tag{7}$$

where P is the target return power (without background), M is the detector internal gain factor, and R denotes the detector's responsivity given in A W^{-1}. For the mean current fluctuation we derived the following expression:

$$\langle \Delta I^2_N\rangle = B\left(2eM^2FR(P + P_{\mathrm{back}}) + i^2_D + i^2_0\right)$$

$$+\frac{4k_BT}{R_F} + \left(\frac{u_0}{R_F}\right)^2\right) + \frac{B^3}{3}\left(u_0 2\pi C_{\mathrm{det}}\right)^2 . \tag{8}$$

In this equation, B is the electrical bandwidth, e the elementary charge, F the detector's excess noise factor which accounts for additional noise due to the internal amplification statistics, and i^2_D the dark current noise density. The noise contributions resulting from the electrical amplification process are expressed through the amplifier input current noise density i^2_0, the feedback resistor R_F, the absolute temperature T, and the input voltage noise density u^2_0. C_{det} accounts for the equivalent capacity of the detector including the capacities of the amplifier input and wirings. P_{back} in (8) is the background signal which originates from other sources such as the reflected or scattered solar radiation or thermal emission dependent on the spectral region, both not fully removed by the spectral filter in the receiver channels. It can also contain contributions from the dark current. For a noise-free detector with the quantum efficiency and excess noise factor equal to unity, CNR of (7) simplifies to

$$\mathrm{CNR}^{\mathrm{ideal}} = \frac{P}{\sqrt{2h\nu B(P + P_{\mathrm{back}})}}, \tag{9}$$

where shot noise from the hard target reflection and background radiation basically limit the detector performance. In this equation $h\nu$ is the energy of a single photon emitted at frequency ν and h is Planck's constant.

The influence of speckle noise on the performance of a direct detection instrument can be estimated from examination of the number of statistically independent spatial and temporal speckle cells falling on the receiver aperture. For a Gaussian beam profile, the speckle-related signal-to-noise ratio SNR_s is approximately given in [33]:

$$\mathrm{SNR}_s \cong \frac{\pi}{\lambda}\vartheta_L R_T\sqrt{\frac{\tau_r}{\tau_c}}. \tag{10}$$

In this equation, ϑ_L denotes the half cone beam divergence of the transmitted radiation, R_T is the radius of the collecting telescope, τ_c is the coherence time of the laser pulse, and τ_r is the sampling time.

The terms $\pi\vartheta_L R_T/\lambda$ and $\sqrt{\tau_r/\tau_c}$ of (10) denote the improvements from spatially and temporally averaging, respectively. For a Fourier transform limited laser pulse (single longitudinal mode, no chirp), the coherence time is equal to the laser pulse duration. Laser emission in several longitudinal and transversal modes or in the case of variation of the optical length of the laser resonator during the laser pulse would cause a chirp which decreases the temporal coherence considerably. If speckle noise is taken into account, the overall SNR of a direct detection instrument will be given by [34]

$$\mathrm{SNR} = \frac{\mathrm{CNR}}{\sqrt{\left(1 + \frac{\mathrm{CNR}^2}{\mathrm{SNR}^2_s}\left(1 + \frac{1}{(\mathrm{SNR}^L)^2}\left(1 + \mathrm{SNR}^2_s\right)\right)\right)}}, \tag{11}$$

where a coupling between speckle noise and detection noise due to pulse energy fluctuation is taken into account. If the latter can be neglected, (11) will simplify to an expression where

the variances from speckle and detection noise add geometrically. A typical lidar setup that uses direct detection allows for averaging of a large number of statistically independent speckle cells such that the relation $SNR_s \gg CNR$ is fulfilled, and hence the overall SNR is given by the carrier-to-noise ratio defined in (7).

3.3   *Coherent detection instruments*

In contrast to direct detection systems, the return power estimate using a coherent detection principle largely suffers from low SNR_s. This type of instrument requires a diffraction limited system setup, where to first order only one speckle cell is imaged onto the detector surface. In such a setup, SNR_s approaches unity, as can be derived from (10) when a Gaussian beam profile with $\vartheta_L R_T = \lambda/\pi$ and a sampling time $\tau_r = \tau_c$ are used.

In the following we briefly introduce the heterodyne detection principle using the notation from direct detection instruments above. In a heterodyne detection unit, the return power estimate is obtained from the power spectrum of the beat signal generated by mixing the light of a frequency-shifted local oscillator (LO) with the signal of the lidar echo from a pulsed or continuous-wave (cw) laser transmitter [35]. The beat signal is generated by focusing both signals onto a photodetector which is assumed to respond linearly with respect to the return power (i.e. quadratic in the electromagnetic field). The resulting photocurrent has components which are proportional to the target return power P, the local oscillator power P_{LO}, and a periodic signal $2R\sqrt{\eta_{tot}}\sqrt{P}\sqrt{P_{LO}}\cos(2\pi(\nu_S - \nu_{LO})t + \varphi_{rand})$ resembling the output current at the beat frequency $2\pi(\nu_S - \nu_{LO})$ when Doppler shifts are negligible. The frequencies ν_S and ν_{LO} denote the laser transmitter and LO frequencies, respectively, t is the time and φ_{rand} a random phase. The term η_{tot} denotes the cumulative efficiency factor given by the product of the optical, transmitter, and coherent efficiencies and R is the responsivity introduced in (7).

In the next processing step the absolute square of the Fourier transform of the beat signal has to be calculated to estimate the signal contribution at frequency $2\pi(\nu_S - \nu_{LO})$. This gives the expression $\langle \hat{I}_S^2 \rangle = 2\eta_{tot}R^2 PP_{LO}$ for the power spectrum of the detector current at the beat frequency, which is proportional to the target return power P (the factor of two arises from combining positive and negative frequency contributions). Since the LO signal power is much larger than the return power from the lidar echo, the system noise arises mainly from shot noise of the LO. According to (8), the noise term can be expressed by $\langle \Delta \hat{I}_N^2 \rangle = 2eRP_{LO}B$ when a PIN diode with $M = F = 1$ is used as the photodetector and the shot noise from the LO dominates all other noise sources of the detector. Since in a heterodyne setup only one speckle of the incoherent backscattered radiation is imaged, the return power P is a random variable where the corresponding electrical fields are described by a Gaussian statistical process with zero mean. The same holds true for the fluctuations of the LO radiation. The Fourier transform converts these real Gaussian processes to complex ones in the frequency domain. Now, the absolute square of a complex Gaussian process follows an exponential distribution. For exponential distributions in general

the standard deviation is equal to the mean, so that we finally obtain $\sqrt{\langle \Delta \hat{I}_S^2 \rangle} = \langle \hat{I}_S^2 + \Delta \hat{I}_N^2 \rangle$ for the standard deviation of our power spectrum estimate of the combined fluctuations from the backscatter signal and the LO [36]. From this and the signal power to noise density ratio $PND = B\langle \hat{I}_S^2 \rangle / \langle \Delta \hat{I}_N^2 \rangle$ it follows that the overall SNR for a single shot and a single range gate can be expressed by

$$SNR \equiv \frac{\langle \hat{I}_S^2 \rangle}{\sqrt{\langle \Delta \hat{I}_S^2 \rangle}} = \frac{1}{1 + \dfrac{eB}{\eta_{tot}RP}} = \frac{1}{1 + \dfrac{B}{PND}} \,, \qquad (12)$$

with $PND = \eta_{tot}RP/e$. The responsivity R is related to the quantum efficiency Q of the photodetector by the equation $R = Qe/h\nu$. Using this substitution, the signal power noise density ratio is given by $PND = Q\eta P/h\nu$, an expression more frequently found in the literature. From (12) it follows that SNR approaches unity for $PND \gg B$ and $SNR = 0.5$ when $Q\eta P = h\nu B$ reaches the threshold limit. In the latter case, the effective target return power which includes all losses in the heterodyne receiver is equal to the quantum noise limit expressed by the product of photon energy and bandwidth. In any case, the SNR is always smaller than unity; thus, a large number of statistically independent shots have to be accumulated along the track direction to obtain a small random error of the greenhouse gas optical depth expressed by (6). Furthermore, the coherence time τ_c of the pulsed laser transmitter should be fitted to the bandwidth by the relation $B\tau_c \approx 1$ to obtain a high efficiency factor [35].

A cw IPDA lidar system utilising the coherent detection principle combines the advantage of a small receiver bandwidth with a narrow-band laser spectral width. Such an instrument flying over a scene will see a time-varying speckle pattern which depends on two parameters, the aperture diameter D_0 of the receiving telescope and the satellite velocity v_{sat}. If a statistically independent speckle pattern per $D_0/2$ motion of the spacecraft is assumed, the speckle bandwidth will be given by $B_{cw} = 2v_{sat}/D_0$. Substitution of B by B_{cw} in (12) and averaging over TB_{cw} speckles yields

$$SNR_{cw} = \sqrt{TB_{cw}}\,\frac{1}{1 + \dfrac{B_{cw}}{PND}} \,, \qquad (13)$$

with T being the total integration time of the observation along the track direction. The speckle bandwidth B_{cw} is approximately 15 kHz for a 1-m and 30 kHz for a 0.5-m telescope aperture in the case of a LEO (low Earth orbit) with an orbit velocity of about 7 km/s.

3.4   *Results*

Promising candidate absorption lines in the infrared spectral region have been identified around 1.57 μm and 2.05 μm for CO_2, 1.65 μm and 2.29 μm for CH_4, and 3.93 μm for N_2O with the help of an IPDA performance simulation tool [29]. An overview of the optimum on- and off-line positions found is given in Table 1. The frequencies selected are the result of a compromise between small temperature dependency and water vapour cross sensitivity on the one hand,

and appropriate weighting function and optical depth for high measurement sensitivity on ground on the other hand. For low-noise detectors such as avalanche photodiodes (APDs) with a noise equivalent power (NEP) value of 10 fW/$\sqrt{Hz}$ an optimum one-way optical depth (OD) of around ~ 1.2 was found, whereas for PIN diodes with a NEP of 200 fW/$\sqrt{Hz}$ smaller ODs of around 0.6–0.7 are more appropriate. Since the solar background radiation is low for wavelengths larger than 1.3 μm this played a minor role in the selection of these lines. A critical selection aspect was the avoidance of interference by other trace gases, especially water vapour. Isotopic lines were not considered.

Figure 3 illustrates the total atmospheric optical depth for a vertical path in the vicinity of the selected absorption lines. The line-by-line atmospheric transmission calculations assume trace gas volume mixing ratios at the surface of 410 μmol/mol for CO_2 (expected global mean value in 2015–2020; assumed to be constant with altitude), 1700 nmol/mol for CH_4, and 320 nmol/mol for N_2O. The spectra were computed for US standard atmosphere conditions and include the most relevant interfering trace gases. The HITRAN'96 (HITRAN 2004 for water vapour) [37] database was used to compute the absorption cross sections of all lines of the main isotope lying in the selected spectral region. To model the spec-

tral absorption features under atmospheric conditions, a Voigt line profile has been assumed for each individual absorption line to account for collisional and Doppler broadening effects [38]. Figure 3b illustrates how a careful selection of the off-line position may cancel the spectroscopic water vapour dependency, by choosing the same H_2O absorption level as for the on-line position.

The calculation of the amount of reflected radiation for IPDA requires estimates of the surface reflectivity for the selected wavelengths. In this study, representative values, listed in Table 2, have been taken from moderate-resolution imaging spectroradiometer (MODIS) data over vegetation following [32]. The water reflectivity is deduced from the same study, by sun glitter reflectance histograms obtained from polarization and directionality of the Earth's reflectances (POLDER) data. The median ocean reflectivity of 0.08 (for 1.6–2.3 μm) in the nadir viewing direction corresponds to an average oceanic wave amplitude of 10 m and a mean wind speed of 10 m/s. The LibRadtran radiative transfer calculation tool [39] was used to estimate the amount of background radiation P(back) affecting the CNR of the direct detection instrument as expressed in (8). This is the sum of radiation emitted by the Sun and the Earth, scattered onto the detector by air molecules, aerosol and cloud particles, and the surface.
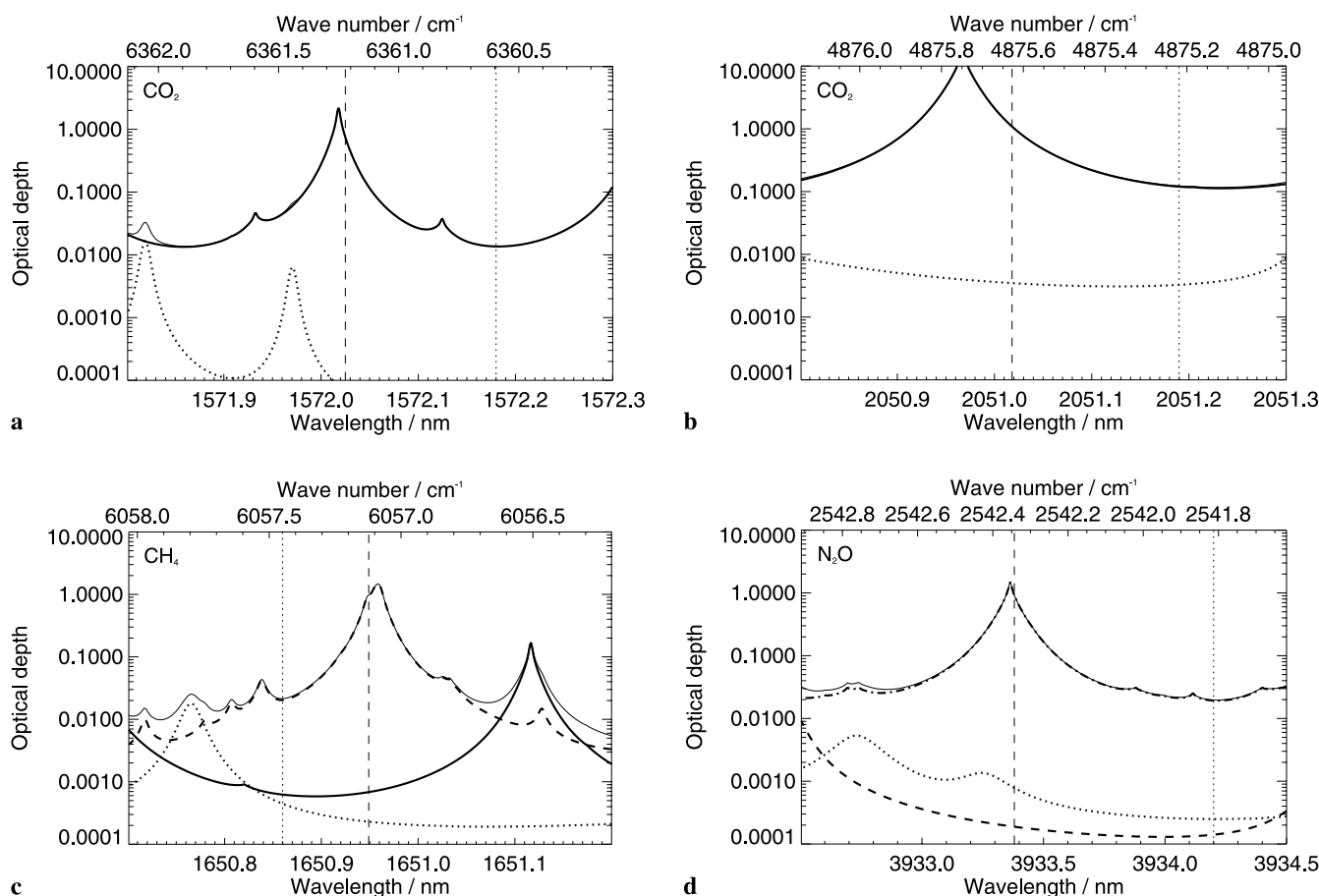

FIGURE 3   One-way trace gas optical depths of the standard atmosphere vertical column up to 65-km altitude as function of wavelength and wave number for (**a**) CO_2 at 1.57 μm, (**b**) CO_2 at 2.05 μm, (**c**) CH_4 at 1.65 μm, and (**d**) N_2O at 3.93 μm. The total optical depth (sum over all trace gases under investigation, plus water vapour) is the *thin solid line*. *Thick solid*: CO_2, *dotted*: H_2O, *dashed*: CH_4, *dash-dotted*: N_2O. *Thin vertical dashed lines*: on-line positions of Table 1; off-line positions *dotted*. In (**a**) the on-line (off-line) optical depth of water vapour amounts to 8×10^{-5} (2×10^{-5})

Instrument parameter	Direct detection Pulsed	Heterodyne detection Pulsed	cw
Transmitter			
Effective pulse length [ns][a]	75	75	–
Double pulse rep. rate [Hz]	50	7500	–
Pulse energy, power monitor prec.	0.1%	0.1%	0.1%
Receiver			
Telescope diameter [m]	1.5	1.0	0.5
Field of view (full angle; µrad)	250	2	1
Opt. efficiency including filter	41%	–	–
Overall heterodyne efficiency	–	15%	15%
Optical filter bandwidth [nm]	1	Not req.	Not req.
Detector and amplifier			
Type	APD[b]	PIN	PIN
Internal gain	20	1	1
Excess noise factor	4.3	1	1
Quantum efficiency	80%	70%	70%
Amplifier bandwidth [MHz]	3	–	–
Speckle bandwidth[c] [kHz]	–	–	28.6
Noise equivalent power[d] [fW/$\sqrt{}$Hz]	APD: 24 PIN: 480	–	–
Platform and atmosphere			
Orbit altitude and velocity		450 km, 7.14 km/s	
Orbit type		6 h/18 h sun-synchronous	
Viewing geometry		Nadir	
Atmosphere model		US standard atmosphere	
Aerosol model		Median aerosol profile[e]	
Surface reflectivity over ocean/vegetation	1.6 µm	0.08/0.31	
	2.0–2.3 µm	0.08/0.09	
	3.9 µm	0.02/0.02	
Nadir radiance[f] over ocean/vegetation [mW/(m² nm sr)]	1.6 µm	1.7/5.0	
	2.0–2.3 µm	0.5/0.5	
	3.9 µm	0.4/0.4	

TABLE 2 Instrument parameters for state-of-the-art direct and coherent detection IPDA instruments and environment conditions for a space-borne platform following [29]

[a] From (3)
[b] Avalanche photodiode (APD) for $\lambda < 2.0$ µm, otherwise PIN diode
[c] See (12)
[d] Assuming a detector–amplifier chain with a detector dark current noise density of 160 fA/Hz$^{1/2}$, an amplifier input current (voltage) noise density of 4 fA/Hz$^{1/2}$ (3 nV/Hz$^{1/2}$), an amplifier temperature of 300 K, an equivalent input capacity including wiring of 4 pF, and a feedback resistor of 1 MΩ
[e] From [29]
[f] For a solar zenith angle of 75° using [39]

It depends on the viewing direction, the solar zenith angle, the surface reflectivity, and the wavelength. An aerosol optical depth of 0.03 was assumed for modelling the aerosol influence in the background radiation at 1.6 µm [39]. To minimise solar background radiation while assuring continuous solar power for the satellite, a sun-synchronous dawn–dusk orbit would be ideal. From statistical analysis of possible solar zenith angles for such an orbit over a period of one year, it was found that a solar zenith angle of 75° (worst case is 60°) covers most of the cases. The resulting background radiation is listed in Table 2, valid for the cloud-free US standard atmosphere and the surface reflectivity indicated.

Figures 4–6 show results from sensitivity analyses when detector and atmospheric parameters are varied. The random error profiles as a function of target altitude allow estimating the performance in the presence of elevated targets such as mountains or clouds. The reference system (solid line) parameters stem from Table 2. In these computations an orbit height of 450 km and a direct detection instrument measuring CO_2 in the 1.6-µm absorption band (line 'a' from Table 1) were assumed. To improve the SNR, 3570 shot pairs have been averaged, which results in an along-track integration length

of 500 km due to the satellite's velocity of ~ 7 km/s and the double-pulse repetition frequency of 50 Hz of the lidar transmitter. The individual parameter sensitivity can be deduced from the variation range displayed in the figures. For the reference system the random error of the total CO_2 column number density is $\sim 0.04\%$. The value is not optimised with respect to the user requirements, since this exercise was solely dedicated to investigate the sensitivity of individual parameters to the overall system performance under realistic instrument and environment conditions.

It turns out that among all instrument parameters the detector dark current (Fig. 4c) is the most critical one where performance improvements could lead to substantial relaxation of the size of the instrument for comparably low random error. The bandwidth of the optical filter and the field of view of the collecting telescope, both influencing the background radiation level on the detector, are uncritical parameters as long as the detector dark current limits the measurement performance. Variations of the transmitter pulse energy behave like variations of the telescope size in Fig. 4a and are therefore not shown explicitly. A variation of the background radiation level has, like the variation of the filter bandwidth shown in
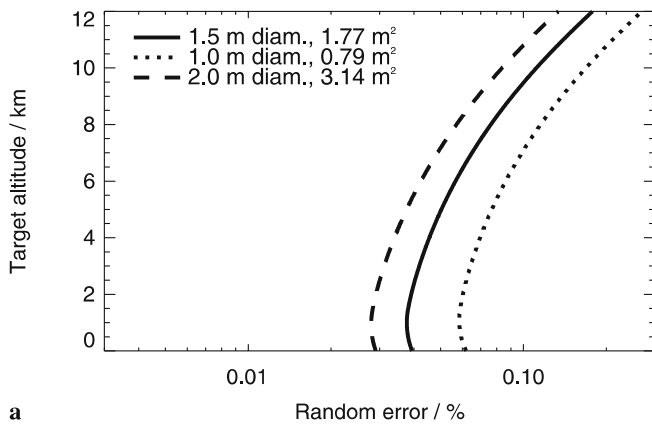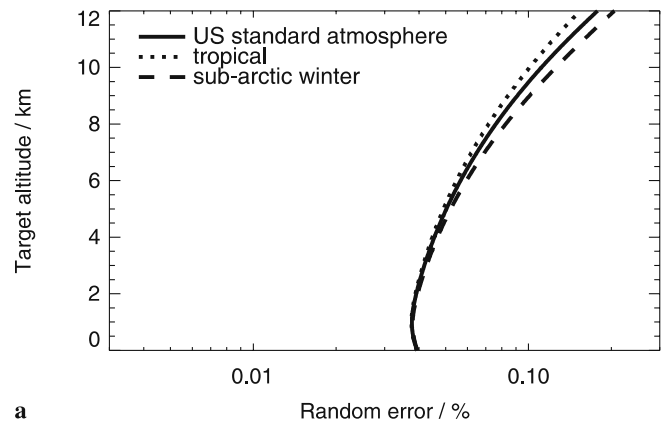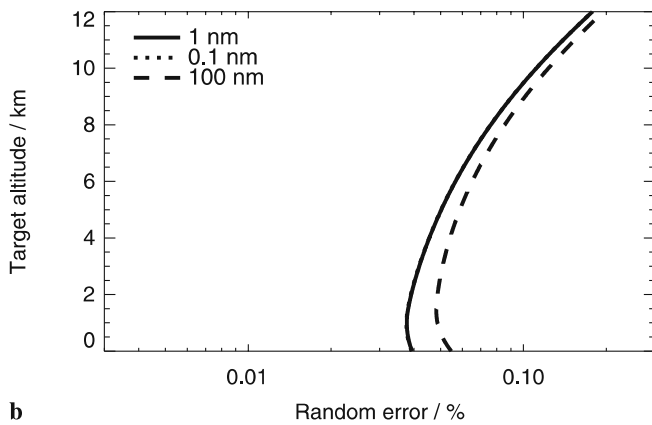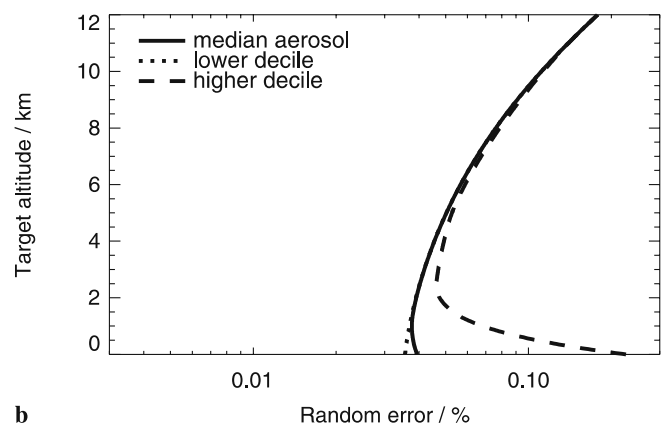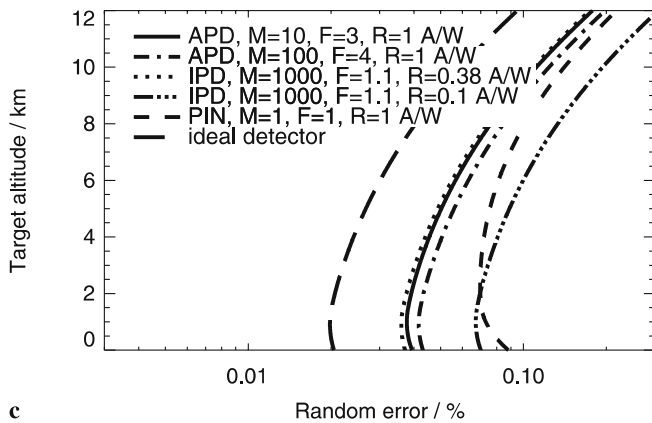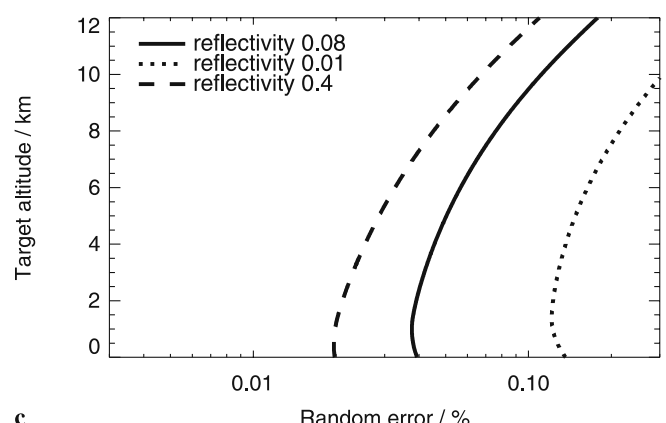
FIGURE 4 Relative CO_2 column number density error at $1.57\,\mu m$ for 500-km horizontal integration as function of target altitude and varied detector parameters: (**a**) telescope diameter, (**b**) receiver filter bandwidth (FWHM), (**c**) semiconductor type. Variations of the transmitter pulse energy behave like (**a**) and are therefore not shown explicitly. The reference system (*solid line*) parameters are listed in Table 2

FIGURE 5 Like Fig. 4, for varied atmospheric parameters. (**a**) Model atmosphere, (**b**) aerosol concentration, (**c**) surface reflectivity

Fig. 4b, no significant influence. As illustrated in Fig. 5, a high variability in the random error performance has to be expected from atmospheric aerosol and surface reflectivity changes, whereas soundings in different climates have no impact on the random error. In particular, high aerosol load, sometimes present in the atmospheric boundary layer, will lead to performance degradation due to enhanced extinction.

Figure 6 shows the impact of ice and water clouds on the system's performance. Most importantly, the simulation runs

in Fig. 6b show that thin cirrus clouds known to be present over large parts of the tropics will not lead to large performance degradation. Optically thick mid-level clouds (Fig. 6a) will of course completely attenuate the laser pulse, but the cloud-top return signal may be used to retrieve the CO_2 column above the cloud in the case where its top is flat enough for averaging an appropriate number of shot pairs. The lidar simulations in Fig. 6a were run with water cloud reflectivities derived from LibRadtran radiative transfer calculations [39]. The reflectivity of a water cloud is mainly dependent on the effective cloud droplet radius and the optical depth. At $1.6\,\mu m$ a water cloud with 10-μm droplet radius and an optical depth
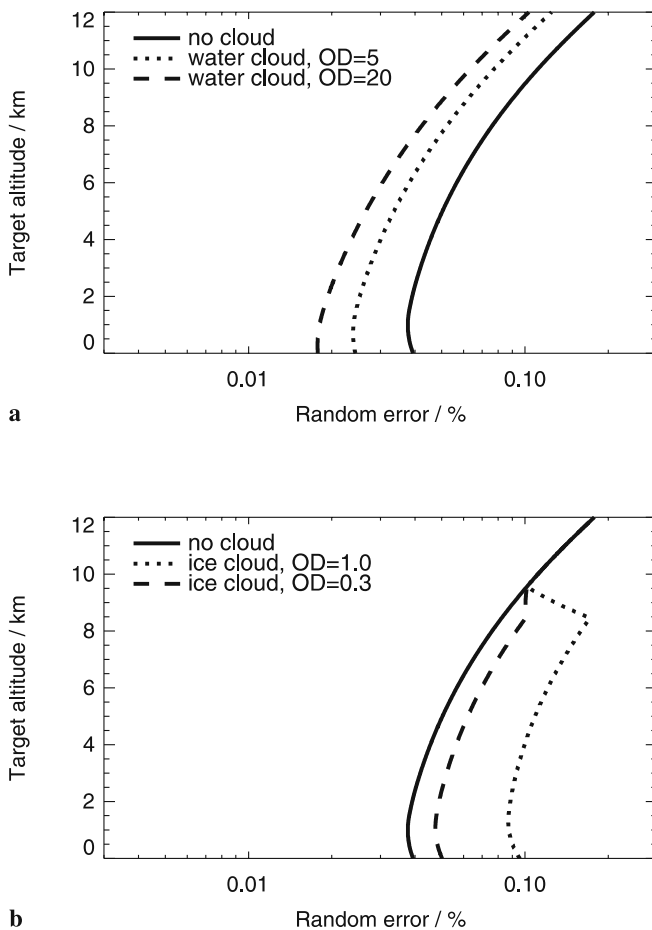
a

b

FIGURE 6 Like Fig. 4, for the presence of clouds. (**a**) Water cloud with effective droplet radius of 10 μm, (**b**) ice cloud (cirrus) between 8.5- and 9.5-km altitude

of 5 (20) has a reflectivity of 0.23 (0.55). We expect IPDA to work even in scattered and complex structured clouds, as well as over extended low-level stratus clouds, when using sophisticated processing methods such as conditional sampling and averaging. This is a considerable advantage over passive sensors that suffer from unknown cloud cover and cloud top altitudes within their larger fields of view.

The sensitivity analyses of Figs. 4–6 served as a base for the definition of a complete system for each instrument given in Table 2. Some of the instrument parameters of this table

have been optimised in size in order to meet the user requirements given in Table 3. In this table, a performance loss by a factor of $\sqrt{2}$ was taken into account due to an assumed 50% cloud coverage on a global average affecting the lidar signals reaching the ground for the total column [26]. The detector parameters of each instrument have been taken from commercially available sources. The parameters of interest are size of the laser transmitter (e.g. laser pulse energy, repetition rate, or the laser power of a cw system) and telescope aperture of the receiver system. In particular, the product of average power (pulsed instrument) and telescope aperture, which balance each other, drives size and cost of a space-based instrument. We tried to select reasonable instrument approaches for the laser systems and telescope apertures that have a certain heritage, e.g. a telescope size of 1.5 m for direct detection IPDA lidar [25]. Considerably smaller telescope apertures (e.g. 1–0.5 m) are possible in case of a heterodyne instrument.

Table 3 lists the resulting transmitter pulse energies for the pulsed systems and power values for the cw systems needed over vegetation or water as a function of the investigated trace gas, the wavelength region, and the most important user requirements (horizontal resolution and precision). As stated above (cf. Figure 4c), the performance of direct detection instruments is mainly limited by the detector dark current. This is even more important at 2 μm where the use of PIN diodes with missing internal amplification degrades the performance. The fact that more favourable weighting functions in the 2-μm region allow us to relax the required precision does not counterbalance this. To fulfil the requirements, direct detection IPDA would need a power–area product of 7.1 and 0.5 W m^2 for CO_2 and CH_4 at 1.6 μm over the ocean and of 10 W m^2 for N_2O at 3.9 μm, regardless of the surface albedo.

The idea in sizing the coherent instruments was to operate them as close as possible near the threshold limit (e.g. $B/PND \sim 1$) where the quantum noise is equal to the effective target return power for the on-line signal. In this case, the SNR of a single shot and a single range gate is close to 0.5 and the overall measurement sensitivity is proportional to the square root of the number of independent shot pairs measured along the track direction of the satellite. For pulsed systems we limit the maximum repetition rate to a value of 7.5 kHz in order to avoid signal ambiguity due to reflections from high-level clouds in the tropics. As a result it was found that the telescope size can be considerably reduced compared to the direct detec-

Species	Wavelength [μm]	Hor. res. [km]	Max. allowed column error	Required pulse energy or power over ocean/vegetation		
				Direct det. Pulsed [mJ]	Heterodyne detection Pulsed [mJ]	cw[a] [W]
CO_2	1.6	50	0.2%	40/9	–[b]	–[b]
	2.1	50	0.4%[c]	80/70	0.150/0.144	3.4/2.9
CH_4	1.6	220	0.4%	3/1	0.020/0.004	0.6/0.2
	2.3	220	0.6%[c]	20/17	0.013/0.011	0.5/0.4
N_2O	3.9	550	0.3%[d]	53/53	0.050/0.050	1.5/1.5

[a] Average power for the cw system
[b] Requirements cannot be met
[c] Favourable weighting function of 2 μm line wing allows relaxing the required precision
[d] Threshold requirements

TABLE 3 Resulting transmitter pulse energy or average power for the direct and coherent detection instruments needed to meet the target (for N_2O: threshold) observational requirements from [29] under instrument and environment configurations listed in Table 2

tion instrument. For a cw IPDA lidar the situation is somewhat different, because the telescope aperture impacts on three parameters as outlined in (13) which need to be optimised. These are (i) the speckle bandwidth given by the diameter of the telescope aperture and the satellite velocity, (ii) the number of independent speckle cells given by the speckle bandwidth and the integration time in the along-track direction, and (iii) the target return power. From analysis it was found that a reasonable combination would be a 0.5-m telescope and a laser power of 3.4 W to meet the observational requirements from Table 3. Alternatively, in the case where the power was the most important cost driver, a telescope of 0.7 (1.0) m diameter would require 1.7 (0.9) W. It is worth mentioning that both the pulsed and the cw heterodyne systems do not fulfil the requirements at 1.6 μm unless an unrealistically large instrument is used.

4 Systematic error

4.1 *Performance model*

Systematic errors of the optical depth expressed by (1) may arise for different reasons: with respect to the atmosphere, errors in the meteorological fields for temperature, pressure, and water vapour lead to errors in computation of the weighting function (5), the air number density, and the dry air mixing ratio of the trace gas under study. Other errors also affecting the total column may be introduced by uncertainties in the path length determination or spectral broadening and frequency drifts of the radiation source used. Uncertainties in the measurements of the relative pulse energies and relative receiver optical efficiencies or non-precise alignment of the overlap between the laser beam and the telescope field of view

are further sources of systematic errors. In Table 4, various error sources and their relative impact on the bias budget of a space-borne IPDA lidar are listed exemplarily for a direct detection instrument measuring CO_2 in the 1.6-μm spectral region. The relative error contribution for each parameter has been estimated from linear expansion of (1) around the true value assuming negligible error correlation, which led to the following expression, for the relative uncertainty of the optical thickness:

$$\frac{\Delta \delta_{gas}^i}{\delta_{gas}} = \left| \frac{1}{\delta_{gas}} \frac{\partial \delta_{gas} \Delta x_i}{\partial x_i} \right| . \tag{14}$$

In this equation, Δx_i stands for the assumed uncertainty of the specific input parameter denoted by the subscript i. The error budget shown in Table 4 results from the geometrical sum of the individual error contributions. In the following paragraphs a more detailed description of the origin of the systematic errors introduced above is given.

4.2 *Atmospheric effects*

For studying systematic errors arising from uncertainties of the temperature and pressure profiles, the reference profile for temperature data was introduced with a temperature of $T_0 = 288.15$ K at sea level, a lapse rate of -6.5 K/km between 0 and 11 km, a constant level of 216.5 K between 11 and 20 km, and an increase of the temperature with a lapse rate of 1 K/km between 20 and 40 km according to the US standard atmosphere. The reference pressure profile was computed from integration of the hydrostatic equation assuming a ground pressure value of 1013.25 hPa, while the density profile was obtained from applying the ideal gas equation. These

Error source	Bias		Assumption or uncertainty for CO_2
	%	μmol/mol	
Atmosphere			
Temperature	0.010	0.035	0.5 °C
Surface pressure	0.032	0.120	0.5 hPa
H_2O mixing ratio	0.023	0.090	5% in the tropics
H_2O line interference	0.001	0.003	20% in the tropics
Aerosol scattering	0.001	0.003	ESA reference model atmosphere (RMA)
Temp. dependence of abs. line parameters			For 0.5 °C temperature bias and T neutral line position
Line strength	0.017	0.065	2% uncertainty
Pressure shift	0.020	0.076	1% uncertainty
Pressure broadening	0.018	0.067	1% uncertainty
Temperature scaling exponent	0.016	0.061	2% uncertainty
Transmitter/Receiver			
Bandwidth	0.002	0.008	15 MHz (FWHM)
Frequency drift	0.028	0.106	0.3 MHz at 1.6 μm
Spectral purity	0.022	0.084	99.9% with 1-GHz filter
Rel. pulse energy calibration (on-, off-line)	0.025	0.095	5×10^{-4} accuracy
Rel. detection channel calibration (on-, off-line)	0.025	0.095	5×10^{-4} accuracy
Path length	0.022	0.084	2 m
Pointing/Timing			
Doppler shift along track	0.028	0.106	0.067 mrad pointing
Doppler shift across track	0.003	0.011	1 mrad pointing
Rel. on-/off-line pointing	0.005	0.019	$\Delta\varrho/\varrho < 10^{-4}$
Temporal interpulse separation (on-/off-line)	0.005	0.019	$\Delta\varrho/\varrho < 10^{-4}$
Error budget	0.08	0.31	Geometrically added

TABLE 4   Estimate of the systematic error contribution of a space-borne direct detection IPDA instrument for the measurement of the CO_2 column content in the 1.6-μm spectral region. The target requirement for the relative systematic error amounts to 0.026% (0.1 μmol/mol) as taken from [29]

profiles served as the input parameters for the calculation of the reference optical thickness using (1). For the variation run the temperature was changed by a constant amount at each height level. The modified temperature profile led to changes both in the air number density and the absorption cross section, and hence gave rise to a systematic error in the total optical thickness. As suggested in [9] and [29], this error can be kept to a minimum if temperature-insensitive absorption lines are selected. Figures 7 and 8 illustrate the situation exemplarily for the two lines 'a' and 'c' of Table 1 where the water vapour line interference was lowest. In the case of line 'a' (1.6-μm spectral region) two temperature neutral frequency positions are found from a displacement of the laser frequency by $\Delta \nu \sim 0.54$ GHz and ~ -0.78 GHz, compared to the line centre position. The asymmetry in the temperature neutral frequency positions is due to the pressure shift parameter of -0.075 cm^{-1}/atm which was used for the cross-section calculations [40]. It is important to note that these frequency positions only slightly change for a different reference profile as depicted in Fig. 7. It is also seen that the frequency neutral points match with an appropriate one-way optical depth
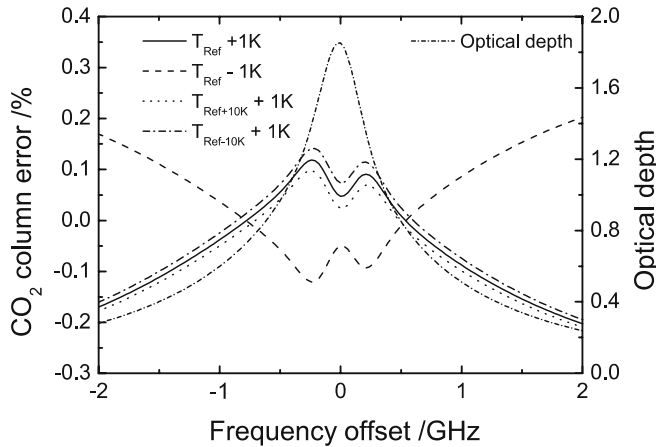

FIGURE 7 Temperature-related CO_2 column error (*left-hand axis*) and optical depth (*right-hand axis*) computed as function of frequency detuning around line 'a' from Table 1 in the vicinity of the temperature neutral points. The *inset* indicates the temperatures selected for the variation run. The *right-hand axis* shows the one-way optical depth
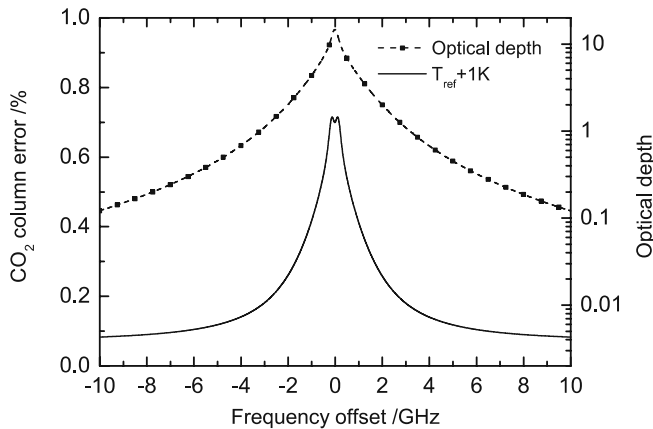

FIGURE 8 Temperature-related CO_2 column error (*left-hand axis*) and optical depth (*right-hand axis*) computed as function of frequency detuning around line 'c' from Table 1. The *inset* indicates the temperatures selected for the variation run. The *right-hand axis* shows the one-way optical depth

of ~ 0.9 for the column measurement and the relative error in the optical depth can be kept well below the target error bound in the case of a temperature uncertainty of 1 K from ground up to 40-km height. For line 'c' (2-μm spectral region) the situation is a little different. As illustrated in Fig. 8, the temperature sensitivity decreases with an increasing frequency displacement from the centre line but does not change sign to reach a temperature neutral point. Using line 'c', a frequency displacement of as much as 2 GHz off line centre would be advantageous because of the favourable weighting function as discussed in Sect. 2.2.

Since not only the temperature profile, but also the absorption line parameters, are known only with certain accuracy, an additional systematic error appears which is due to the combination of these uncertainties. In order to estimate this contribution, the analysis described above has been re-run with line parameters changed by 2% compared to the HITRAN database. Two error contributions were identified. The first leads to a constant bias value in the order of 0.3%, which does not depend on the regional temperature profile. This source of error can in principle be removed by sensor calibration. The second source of error shows a small regional bias of 0.02% if the reference temperature profile is varied and an uncertainty of ± 1 K is assumed for the temperature profile from the variation run. We note that this source of error cannot easily be removed by sensor calibration.

Opposed to the temperature interference which can be kept to a minimum for proper line selection, access to accurate surface pressure data is very demanding. In the case of selection of line 'a' from Table 1, a small surface pressure uncertainty of only 0.5 hPa causes a significant bias contribution in the order of 0.032%. For a weighting function peaking at the ground as shown in Fig. 1 this error contribution is even larger. Further atmospheric bias effects may arise from atmospheric water vapour and aerosols. Biases caused by water vapour are due to both overlapping absorption lines and correction of the optical thickness for the dry air mixing ratio as expressed in (1). An upper bound can be estimated by assuming a worst case tropical water vapour profile for that reference run for which the errors are the largest. It is found that the line interference term amounts to 0.001% only and hence can be neglected. However, an error of 0.022% has to be taken into account for the correction term even in the case where the water vapour data is well known with a precision of 5%. For the study of aerosol effects a median aerosol profile taken from ESA RMA [29] has been used for the variation run. The relative bias contributes only $\sim 0.001\%$ to the total error budget and is therefore negligible.

4.3   *Laser spectral profile*

Systematic errors which may arise from spectral characteristics and possible frequency drifts of the radiation source were investigated by substituting the absorption cross section of (1), which is valid only for monochromatic light, by the effective absorption cross section

$$\sigma_{\text{eff}}(r) = \frac{\left[\int_0^\infty L(\nu - \nu_0)\tau^2(r, \nu)(\sigma(r, \nu - \nu_{\text{on}}) - \sigma(r, \nu - \nu_{\text{off}}))\, d\nu \right]}{\int_0^\infty L(\nu - \nu_0)\tau^2(r, \nu)\, d\nu}. \qquad (15)$$

In this equation, $L(\nu - \nu_0)$ is the spectral energy distribution of the radiation source with its centre frequency ν_L and τ is the atmospheric transmission given by

$$\tau(r, \nu) = \exp\left[-\int_{r_{TOA}}^{r} q_{gas}(r')\left(1 - q_{H_2O}(r')\right) n_{air}(r') \right.$$

$$\left. \times \left(\sigma_{on}(r', \nu) - \sigma_{off}(r', \nu)\right) dr' \right]. \quad (16)$$

For studying the influence from limited bandwidth, a narrow-band radiation source providing ns laser pulses is assumed. The spectral energy distribution is modelled assuming the following laser line shape:

$$L(\nu) = \frac{\pi^2}{b} \frac{1}{2\cosh\left(2\pi^2 \frac{\nu}{b}\right) + 2\cos\left(\pi \frac{a}{b}\right)}, \quad (17)$$

with the parameters $a = 1/4(1/\tau_r - 1/\tau_f)$ and $b = 1/4(1/\tau_r + 1/\tau_f)$. This profile was obtained by Fourier transformation of the function $P(t) \sim e^{2at}/(e^{2bt} + e^{-2bt} + 2)$, which has been assumed as the temporal distribution of the laser pulse, with τ_r and τ_f being the rise time and fall time, respectively. The bandwidth of $L(\nu)$ is given by FWHM $= b/\pi^2 \ln((R + \sqrt{R^2 - 4})/2)$ with $R = 2(2 + \cos(\pi a/b))$. As an example, Fig. 9 depicts three typical laser line shapes which were obtained from calculation of the spectral energy distribution using (17) and a ratio of $\tau_f/\tau_r = 3$ for the rise and fall times [41]. In our simulation a nearly monochromatic laser line (FWHM = 0.1 MHz) was assumed for the reference run. This bandwidth is more than three orders of magnitude smaller than the spectral width of the Doppler-broadened CO_2 absorption line of ~ 300 MHz (FWHM) at $1.6\,\mu$m. For the variation run the bandwidth was varied according to Fig. 9. As shown in Fig. 10 for soundings in the wing of the line, the error induced by the finite bandwidth can be kept well below the target value even for relatively broadband laser sources of up to 50 MHz (FWHM). If soundings in the line centre are preferred the laser bandwidth should not exceed a value of 10 MHz in order to meet the target error bound. It is worth
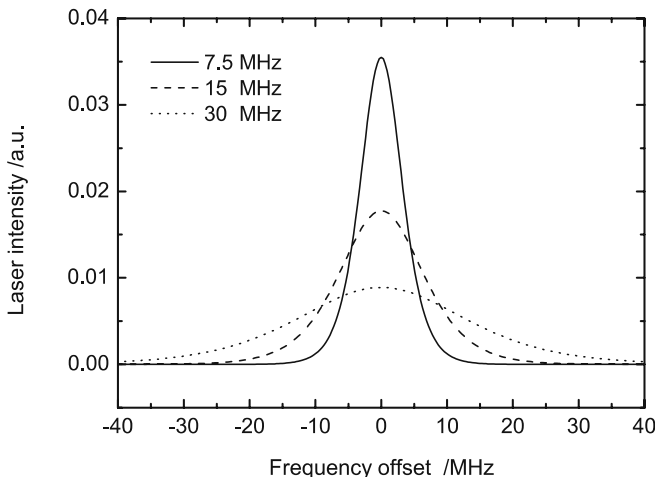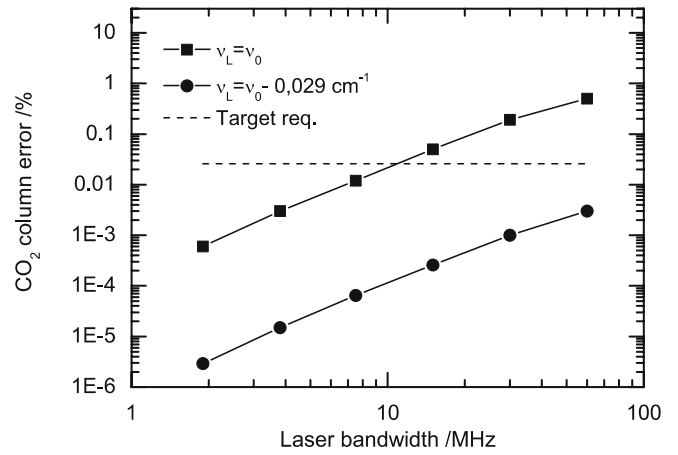

FIGURE 10 Relative CO_2 column error as function of the laser bandwidth (FWHM) for soundings at the line wing (*solid circles*) and line centre (*solid squares*) positions of line 'a' from Table 1. The *dashed line* marks the target observational requirement taken from [29]

mentioning that this would add a constant bias in the order of 0.11%, which can principally be removed by sensor calibration.

The errors induced by a possible frequency uncertainty are illustrated in Fig. 11. In this figure the relative error in the two-way transmission $\Delta\tau/\tau$ divided by two is plotted as a function of the frequency offset from the centre line. This error can be directly translated into a relative measurement error for the optical depth. The transmission has been computed according to $\tau = \int L(\nu - \nu_0)\tau_{r_G}^2(\nu - \nu_0)d\nu$ using (16) and (17), where ν_0 denotes the centre frequency of line 'a' taken from Table 1. In this calculation a bandwidth of 30 MHz was assumed for both the reference and variation runs. For the latter a frequency uncertainty of 0.3, 0.6, and 1.2 MHz was assumed. The dispersive-shaped error curves obtained from each uncertainty parameter reflect the sensitivity (e.g. the derivative) of the optical depth per frequency unit. In the line centre, the sensitivity is almost zero. For a small displacement in either direction it strongly increases up to a maximum value which denotes the turning point of the spectrally resolved op-
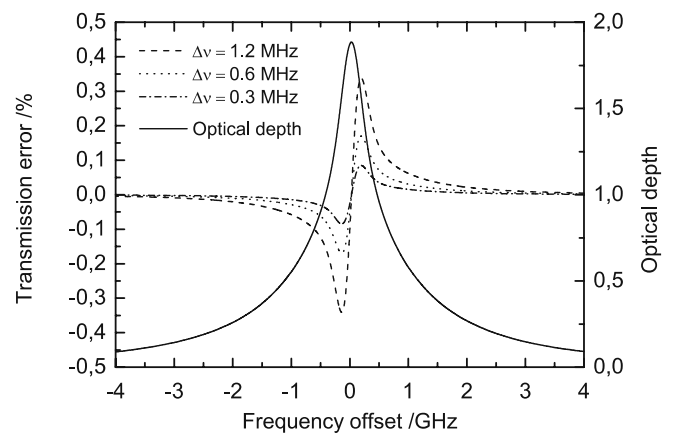

FIGURE 9 Laser intensity as function of frequency offset calculated using (17)

FIGURE 11 Relative transmission error divided by two as function of frequency offset for a frequency uncertainty of 0.3 MHz (*dash-dotted line*), 0.6 MHz (*dotted line*), and 1.2 MHz (*dashed line*). The *right-hand axis* shows the one-way optical depth of line 'a' from Table 1

tical depth. Beyond the region of highest sensitivity, the error in the perturbed transmission decreases for larger frequency displacements. From this analysis it follows that a frequency stability as high as $\sim 0.3/2$ MHz would be required to meet the target error bound for CO_2 soundings at 1.6/2 μm.

As known from previous studies, spurious broadband spectral impurity of the laser line profile can pose significant systematic errors by applying differential absorption lidar [42]. The desired spectral purity value P_{spec} can roughly be estimated using the relation $P_{spec} > 1 - \Delta\sigma/\sigma \exp(-2\delta_{max})$, where $\Delta\sigma/\sigma$ is the maximum tolerable relative cross-section error and δ_{max} is the maximum optical depth [43]. When assuming an ideal one-way optical thickness of $\delta_{max} = 1.1$ and an absorption cross-section error of 0.02% in compliance with the target error bound, an exceptionally high spectral purity $P_{spec} > 99.997\%$ must be met by the laser source. As illustrated in Figs. 12–17, a significant relaxation can be achieved by using a narrow-band optical filter in the receiver path which blocks a significant amount of the unwanted radiation trans-

mitted outside a certain spectral interval. The results shown in these figures have been obtained from estimating the remaining errors using a modified laser line profile $\tilde{L}(\nu) = (1 - P_{spec})L_b(\nu) + P_{spec}L_n(\nu)$ for the variation runs. In this expression $L_b(\nu)$ and $L_n(\nu)$ are normalised functions with respect to their total energy describing the broad- (impure) and narrow-band (pure) parts, respectively. A Lorentzian-type function was assumed for modelling the transmission curve of the narrow-band interference filter in the vicinity of an absorption line. $L_n(\nu)$ was computed using (17) and a value of 30 MHz for the full spectral width. Figure 12 depicts the results for line 'a' where a continuously distributed background emission is assumed for $L_b(\nu)$. A spectral purity of $\sim 99.9\%$ is found sufficient to meet the target error bound in the case where a 1-GHz (FWHM) filter is selected. A 6-GHz optical filter would require a significantly higher spectral purity value of $\sim 99.97\%$. For soundings in the far line wing using line 'c', spectral purity is more relaxed, as depicted in Fig. 15. Figure 16 illustrates another scenario where a frequency comb is
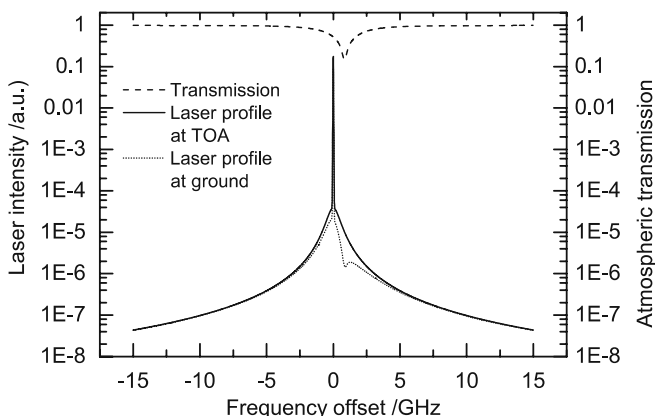

FIGURE 12 Laser spectral profile at top of the atmosphere TOA (*solid line*) and ground (*dotted line*) as function of frequency offset from line wing position of line 'a' from Table 1. The broadband part given by the Lorentzian-shaped filter curve contains the spectral impure background radiation. The atmospheric transmission of line 'a' from Table 1 is shown by the *upper solid line*
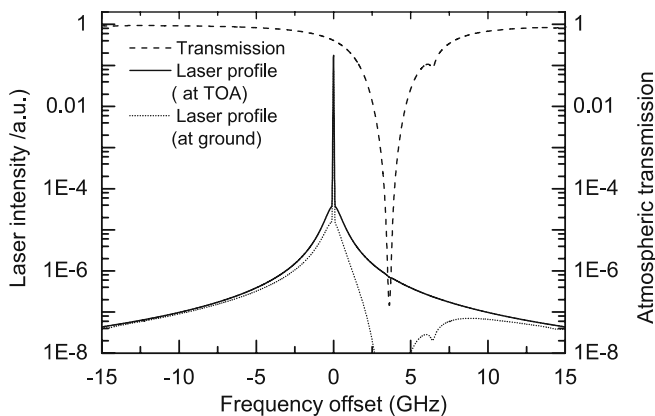

FIGURE 14 Laser spectral profile at top of the atmosphere TOA (*solid line*) and ground (*dotted line*) as function of frequency offset from line 'c' of Table 1. The broadband part given by the Lorentzian-shaped filter curve contains the spectral impure background radiation. The atmospheric transmission of the strong absorption CO_2 line at 2.1 μm is shown by the *upper solid line*
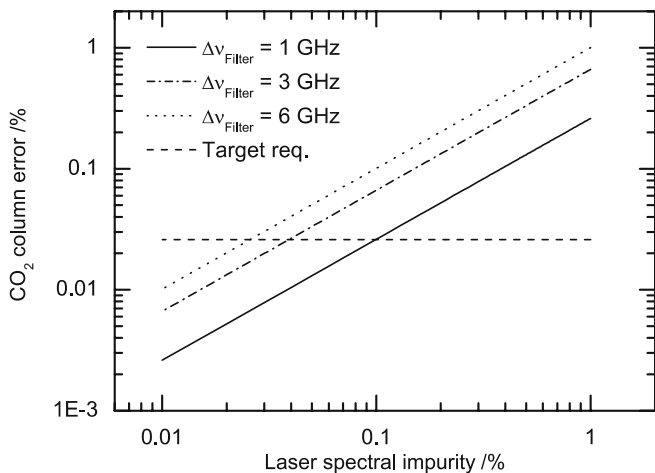

FIGURE 13 Relative CO_2 column error for different filter bandwidths 1, 3, and 6 GHz (FWHM) as function of spectral impurity according to the laser line shape illustrated in Fig. 10 in comparison to the target requirement taken from [29]
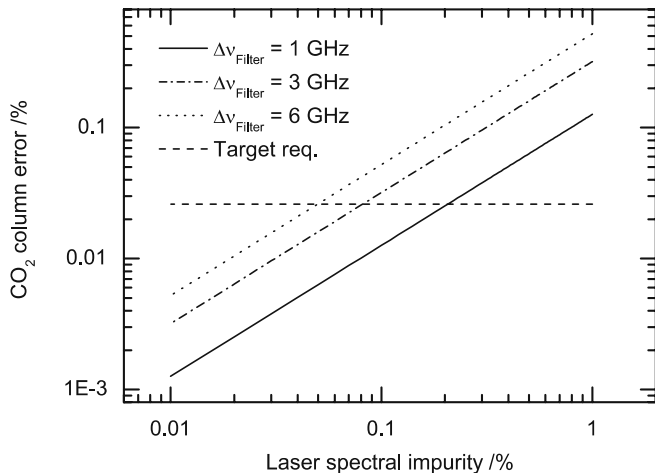

FIGURE 15 Relative CO_2 column error for different filter bandwidths 1, 3, and 6 GHz (FWHM) as function of spectral impurity according to the laser line shape illustrated in Fig. 14 in comparison to the target requirement taken from [29]
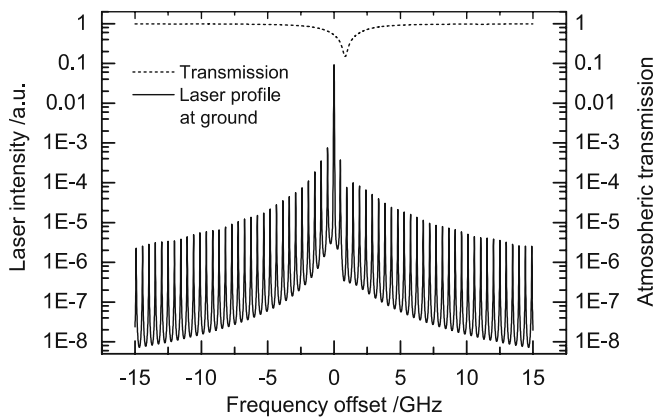
FIGURE 16 Laser spectral profile at ground (*solid line*) as function of frequency offset from line 'a' of Table 1. The spectral impurity is given by a frequency comb modified by the Lorentzian-shaped filter. An Airy function with a FSR of 0.5 GHz is used for describing multi-mode operation. The atmospheric transmission of the weak CO_2 line at 1.6 µm is shown by the *upper dotted line*
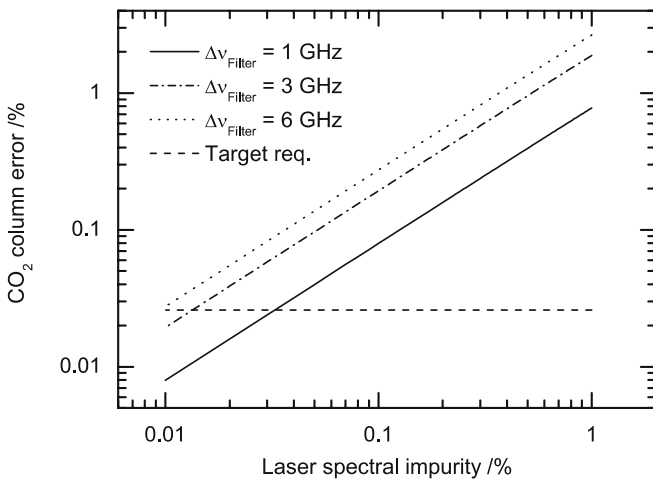

FIGURE 17 Relative CO_2 column error for different filter bandwidths 1, 3, and 6 GHz (FWHM) as function of spectral impurity according to the laser line shape illustrated in Fig. 16 in comparison to the target requirement taken from [29]

introduced for simulating multi-mode operation. Here, $L_b(\nu)$ is modelled by an Airy function with a free spectral range (FSR) of 0.5 GHz. In this example we find that higher spectral purity values of ∼ 99.95% are required to meet the target error bound, even if a 1-GHz (FWHM) filter is used in the receiver path.

4.4   *Further sources of errors*

Further sources of systematic errors may arise from calibration error, misalignment of platform pointing, and errors due to the sounding path length. According to (1) IPDA lidar measurements of the column content require additional information about the relative pulse energy $E_{on,off}$ of the laser pulses from on- and off-line soundings and the relative sensitivity of the receiver channels $D_{on,off}$. From (13) it follows that the relative measurement errors of the parameters $E_{on,off}$, $D_{on,off}$, and the received lidar signals $P_{on/off}$ translate directly into relative errors of the optical thickness by the relations $2\Delta\delta = \Delta E/E = \Delta D/D = \Delta P/P$ if an ideal optical thickness

of $\delta \approx 1$ is assumed. For a low error budget a relative accuracy of < 0.02% is required for each parameter.

The rapidly moving platform ($v \cong 7000$ m/s) leads to a Doppler shift according to $\Delta\nu = \nu_0 v \sin\theta/c$ of the emitted centre frequency ν_0 when the line-of-sight points off-nadir by an angle θ in the along-track direction. A pointing misalignment in the direction of the platform velocity of 0.067 mrad results in a measurement bias of 0.028% for soundings in the line wing. In addition, atmospheric winds ($v \cong 100$ m/s) can lead to a small Doppler shift even in the across-track direction because of the relative motion of the absorbing air parcel with respect to the line-of-sight of the laser beam. A misalignment of the platform by 1 mrad across the track can give rise to a small bias of 0.003%. We note that in this case the Doppler shifts from target echoes are in the opposite direction compared to the transmitted beam. This leads to some relaxation of the pointing stability requirement, when measurements in the line wing positions are performed.

Strongly varying surface reflectivity conditions may also lead to a systematic error in the case where the on- and off-line beams do not point to the same ground spot. The error bounds depicted in Table 4 have been estimated using the relations $2\Delta\delta = \Delta\varphi/\varphi = \Delta\varrho/\varrho$, where $\Delta\varphi$ is the misalignment angle between on- and off-line pointing, φ is the full angle of the laser beam divergence, ϱ is the surface reflectivity, and $\Delta\varrho$ is the difference in the surface reflectances between on- and off-line soundings. A similar amount of error has to be taken into account from temporal interpulse separation between the on- and off-line shots due to the high platform velocity and the limited repetition rate of the pulsed laser. For the error bounds depicted in Table 4 we assumed a change of the surface reflectivity by a factor of two from the moving target and a repetition rate of 100 Hz for the pulsed radiation source.

Since the density of the trace gas is largest near ground, uncertainties in the path length determination have a big impact on the measurement accuracy of the optical thickness. Even a small uncertainty of only 2 m leads to a systematic error in the total optical thickness of 0.022%.

5   Discussion

The parametric studies reveal that both direct and coherent detection principles applied in the near-infrared spectral region promise a high sensitivity for the measurement of the integrated dry air column mixing ratio of the greenhouse gases CO_2, CH_4, and N_2O from a space-borne platform. The measurement performance tends to decrease for wavelengths larger than 2 µm of all investigated instruments. Direct detection sensors suffer from degradation of detector performance when PIN diodes are used and heterodyne detection instruments are in principle limited by speckle noise when operated in the speckle noise limited regime.

IPDA lidar soundings in the wing of absorption lines are advantageous with respect to favourable weighting functions for high sensitivity near ground. This has an impact on the simple two-wavelength approach when considering instruments operating either in the 1.6- or 2-µm spectral regions. In the former case it is found that the required frequency stability needed to meet the target error bound is exceptionally high (∼ 0.3 MHz). This results from the need to run the

system at a frequency displacement close to the line centre for a sufficient optical depth. This stringent instrument requirement can be considerably relaxed by about one order of magnitude when measurements in the 2-μm spectral region are performed. Here, the laser frequency can be tuned to a large frequency displacement $\geq 2\gamma$ for an optimum optical depth where the frequency stability demands are less critical. Nevertheless, to fulfil the frequency stability requirements, sophisticated frequency locking methods would be necessary for both instruments. On the other hand, a laser bandwidth of ~ 30 MHz (FWHM) is not specifically demanding.

A selection of proper sounding frequencies is crucial as it impacts both systematic and random errors. Biases due to erroneous temperature profiles can largely be avoided by use of temperature-insensitive lines and the selection of temperature neutral line wing positions. Using the absorption lines from Table 1, other systematic errors which may arise from line interference of water vapour and other trace gases can be kept to a minimum.

A special situation appears for CO_2 where the stringent target observational requirements cannot be fulfilled by applying coherent detection instruments in the 1.6-μm spectral region. This is different in the 2-μm spectral region where strong absorption lines enable soundings even in far line wing positions. The favourable weighting function leads to a significant relaxation of the target observational requirement by as much as a factor of two as derived in [29]. For direct detection instruments we find that the spectral purity requirement of the transmitted beam is of considerable concern. The amount of impurity tolerable in an IPDA lidar measurement depends on several factors such as the optical depth of the sounding atmosphere, the specific characteristics of the broadband radiation emitted in the vicinity of the sounding frequency, as well as the spectral bandwidth and transmission curve of the optical filter in the receiver channel. Among these parameters, the spectral characteristic of this spurious broadband emission seems to be the most unknown parameter which critically depends on the specific design of the radiation source and which cannot be measured in a direct way. The results above suggest using a 1-GHz (FWHM) filter in front of the detector which will lead to a significant relaxation of the spectral purity requirement by more than one order of magnitude. In this context it is worth noting that coherent detection instruments do not suffer from spectral impurity emission.

Since IPDA lidar instruments are not free from calibration needs, accurate monitoring of the transmitted energy per pulse and receiver optical efficiency which may be different for the on- and off-line frequencies are important issues. Further investigations are needed for the sounding path length where a measurement accuracy of a few metres is desirable even over inhomogeneous regions with strongly varying surface heights. Determination of the sounding path length is particularly challenging for coherent instruments where a large number of shots have to be accumulated even over inhomogeneous terrain before taking the ratio for calculation of the optical depth. The combination of a cw IPDA lidar for the optical depth and a pulsed incoherent backscatter lidar for detection of aerosols and clouds as well as determination of the sounding path length could be a promising payload. Other methods

such as the use of modulation and demodulation techniques are further options to infer range information and to discard unwanted signals from atmospheric scattering in the case of a cw system.

Some drawbacks associated with the use of IPDA lidar for greenhouse gas monitoring are due to the need for auxiliary data such as the surface pressure as well as atmospheric water vapour and temperature profiles. The latter does not seem critical as this kind of information can be obtained from re-analysis data archived at weather centres. More stringent requirements exist for the water vapour profile particularly in the tropical boundary layer where most atmospheric water vapour resides. Accurate knowledge of the surface pressure is a prerequisite for extracting the CO_2 mixing ratio from differential absorption measurements.

IPDA lidar sensors are expected to complement thermal infrared sounders due to their favourable weighting functions peaking in the low troposphere. Passive instruments operating in the solar backscatter region would benefit from global coverage provided by IPDA sensors as they can measure even under night-time conditions and at high latitudes which are not illuminated by the Sun. Further advantages are based on the fact that IPDA lidar measurements do not suffer from unknown aerosol scattering and interference from optically thin clouds not properly detected by passive instruments.

6   Summary

In this study the measurement sensitivity for monitoring of the greenhouse gases CO_2, CH_4, and N_2O by space-borne active remote sensing has been analysed. Performance models for simulation of the random errors of the optical depth to derive the column integrated dry air volume mixing ratio have been implemented for parametric studies. It was found that the method of IPDA (integrated path differential absorption) lidar incorporating direct and coherent detection principles for the ground return enables high detection sensitivity even at a worst case surface reflectivity of 2% for N_2O and signal degradation due to aerosol layers or cirrus cloud coverage. Soundings in the vibration–rotational bands around 1.6 and 2.1 μm were found adequate for monitoring CO_2, the spectral regions at 1.6 and 2.3 μm are suited for CH_4, and wavelengths around 3.9 μm can be used for N_2O measurements. In these spectral regions suitable absorption lines have been identified where line interference from other trace gases, notably water vapour, and systematic errors due to an erroneous temperature profile can be kept to a minimum. Soundings at frequency positions in the wing of the absorption line lead to a high sensitivity in the low troposphere due to the shape of the weighting function which, for this case, peaks near ground.

The simulations indicate that for CO_2 and CH_4 the following stringent target observational requirements for the relative random error can be met: 0.2% for CO_2 and 0.4% for CH_4 for soundings at 1.6 μm, as well as 0.4% for CO_2 at 2.1 μm and 0.6% for CH_4 at 2.3 μm. The IPDA instruments considered in the simulation are expected to be of moderate size in terms of the required telescope aperture (0.5–1.5 m) and laser average power (0.4–4 W). For N_2O, only the threshold requirements (0.3%) could be met. For direct detection instruments it was

found that the risk level increases for wavelengths $> 2\,\mu m$ mainly due to the decreasing detector performance. Coherent detection sensors are limited by speckle noise due to the limited number of independent measurements over the accumulation scene of 50–500 km. An upper limit of the accumulation frequency was given by 7.5 kHz for the pulsed and 15–30 kHz – depending on the telescope aperture – for the cw system.

For CO_2, a systematic error budget of 0.08% was derived from the geometric sum of the individual relative error contributions and from initial assumptions about the required accuracy of all investigated parameters. With respect to the instrument's performance, stringent requirements have to be met for the frequency stability of the laser source (± 0.3 MHz at $1.6\,\mu m$, ~ 2 MHz at $2\,\mu m$) and spectral filtering (~ 1 GHz). With respect to auxiliary atmospheric parameters, the need for accurate surface pressure data (0.5 hPa) has been identified as the most important requirement.

Thanks to both high measurement sensitivity and low systematic errors, we believe that space-borne IPDA lidar systems have a huge potential to complement passive sensors. Infrared sensors measuring the thermal emission at longer wavelengths would have their maximum sensitivity in the middle and upper troposphere. Combining them with an IPDA lidar could give information on the total column not achievable from only one sensor alone. Passive sensors measuring the reflected sunlight from the Earth's surface and clouds suffer from loss of data at high solar zenith angles, particularly in the winter hemisphere at middle and high latitudes.

REFERENCES

1 J. Houghton, Y. Ding, D.J. Griggs, M. Noguer, P.J. van der Linden, D. Xiaosu, *IPCC Third Assessment Report on Climate Change* (Cambridge University Press, New York, 2001)
2 S. Houweling, F.-M. Breon, I. Aben, C. Rödenbeck, M. Gloor, M. Heimann, P. Ciais, Atmosph. Chem. Phys. **4**, 523 (2004)
3 K.R. Gurney, R.M. Law, A.S. Denning, P.J. Rayner, D. Baker, P. Bousquet, L. Bruhwiler, Y.H. Chen, P. Ciais, S. Fan, I.Y. Fung, M. Gloor, M. Heimann, K. Higuchi, J. John, T. Maki, S. Maksyutov, K. Masarie, P. Peylin, M. Prather, B.C. Pak, J. Randerson, J. Sarmiento, S. Taguchi, T. Takahashi, C.W. Yuen, Nature **415**, 626 (2002)
4 A. Chédin, R. Saunders, A. Hollingsworth, N. Scott, M. Matricardi, J. Etcheto, C. Clerbaux, R. Armante, C. Crevoisier, J. Geophys. Res. **108**, 4064 (2003)
5 R.J. Engelen, G.L. Stephens, J. Appl. Meteorol. **43**, 373 (2004)
6 S. Houweling, W. Hartmann, I. Aben, H. Schrijever, J. Skidmore, G.-J. Roelofs, F.-M. Breon, Atmosph. Chem. Phys. **5**, 3003 (2005)
7 M. Buchwitz, R. de Beek, J.P. Burrows, H. Bovensmann, T. Warneke, J. Notholt, J.F. Meirink, A.P.H. Goede, P. Bergamaschi, S. Körner, M. Heimann, A. Schulz, Atmosph. Chem. Phys. **5**, 941 (2005)
8 D. Crisp, R.M. Atlas, F.M. Bréon, L.R. Brown, J.P. Burrows, P. Ciais, B.J. Connor, S.C. Doney, I.Y. Fung, D.J. Jacob, C.E. Miller, D. O'Brien, S. Pawson, J.T. Randerson, P. Rayner, R.J. Salawitch, S.P. Sander, B. Sen, G.L. Stephens, P.P. Tans, G.C. Toon, P.O. Wennberg, S.C. Wofsy, Y.L. Yung, Z. Kuang, B. Chudasama, G. Sprague, B. Weiss, R. Pollock, D. Kenyon, S. Schroll, Adv. Space Res. **34**, 700 (2004)
9 R.T. Menzies, D.M. Tratt, Appl. Opt. **42**, 6569 (2003)
10 J. Bufton, T. Itabe, L.L. Strow, L.C. Korb, B.M. Gentry, C.Y. Weng, Appl. Opt. **22**, 2592 (1983)
11 N. Sugimoto, A. Minato, Appl. Opt. **32**, 6827 (1993)
12 R.A. Baumgartner, R.L. Byer, Appl. Opt. **17**, 3555 (1978)
13 F. Gibert, P.H. Flamant, D. Bruneau, C. Loth, Appl. Opt. **45**, 4448 (2006)
14 M.J.T. Milton, T.D. Gardiner, F. Molero, J. Galech, Opt. Commun. **142**, 153 (1997)
15 A. Minato, D.M.A. Joarder, S. Ozawa, M. Kadoya, N. Sugimoto, Japan. J. Appl. Phys. **38**, 6130 (1999)
16 N. Menyuk, D.K. Killinger, Appl. Opt. **26**, 3061 (1987)
17 A. Fix, G. Ehret, A. Hoffstädt, H.H. Klingenberg, C. Lemmerz, P. Mahnke, M. Ulbricht, M. Wirth, R. Wittig, W. Zirnig, in *Proc. 22nd Int. Laser Radar Conf.*, ESA SP-561, European Space Agency, Paris (2004), p. 45
18 A.I. Karapuzikov, I.V. Ptashnik, O.A. Romanovskii, O.V. Kharchenko, I.V. Sherstov, Atmosph. Ocean. Opt. **12**, 350 (1999)
19 G.J. Koch, B.W. Barmes, M. Petros, J.-Y. Beyon, F. Amzajerdian, J. Yu, R.E. Davis, S. Ismail, S. Vay, M.J. Kavaya, U.N. Singh, Appl. Opt. **43**, 5092 (2004)
20 E.R. Murray, J.E. van der Laan, J.G. Hawley, Appl. Opt. **15**, 3140 (1976)
21 J. Altmann, W. Lahmann, C. Weitkamp, Appl. Opt. **19**, 3453 (1980)
22 J.D. Spinhirne, S.P. Palm, W.D. Hart, D.L. Hlavka, E.J. Welton, Geophys. Res. Lett. **32**, L22S03 (2005)
23 M.J. McGill, L. Li, W.D. Hart, G.M. Heymsfield, D.L. Hlavka, P.E. Racette, L. Tian, M.A. Vaughan, D.M. Winker, J. Geophys. Res. **109**, D07203 (2004)
24 Rep. Assess. ESA SP-1257(1), European Space Agency, September 2001
25 A. Stoffelen, J. Pailleux, E. Källén, J.M. Vaughan, L. Isaksen, P. Flamant, W. Wergen, E. Andersson, H. Schyberg, A. Culoma, R. Meynart, M. Endemann, P. Ingmann, Bull. Am. Meteorol. Soc. **86**, 73 (2005)
26 Rep. Assess. ESA SP-1257(2), European Space Agency, September 2001
27 E.E. Remsberg, L.L. Gordley, Appl. Opt. **17**, 624 (1978)
28 F. Gibert, P.H. Flamant, C. Loth, D. Bruneau, in *Sixth Int. Symp. Tropospheric Profiling, Needs and Technologies (ISTP)*, Leipzig, Germany, September 2003, pp. 249–251
29 G. Ehret, C. Kiemle, Final Rep. ESA Study 10880/03/NL/FF (2005)
30 W.B. Grant, Appl. Opt. **21**, 2390 (1982)
31 M.J. Kavaya, R.T. Menzies, D.A. Haner, U.P. Oppenheimer, P.H. Flamant, Appl. Opt. **22**, 2619 (1983)
32 E. Dufour, F.M. Bréon, Appl. Opt. **42**, 3595 (2003)
33 M. Endemann, ESA Rep., Contract No. 4868/81/NL/HP(SC) (1983)
34 R.E. Warren, Appl. Opt. **24**, 3541 (1985)
35 G. Biernson, R.F. Lucy, Proc. IEEE **51**, 202 (1963)
36 B.J. Rye, R.M. Hardesty, Appl. Opt. **36**, 9425 (1997)
37 L.S. Rothman, C.P. Rinsland, A. Goldman, S.T. Massie, D.P. Edwards, J.M. Flaud, A. Perrin, C. Camy-Peyret, V. Dana, J.Y. Mandin, J. Schroeder, A. McCann, R.R. Gamache, R.B. Wattson, K. Yoshino, K. Chance, K. Jucks, L.R. Brown, V. Nemtchinov, P. Varanasi, J. Quant. Spectrosc. Radiat. Transf. **60**, 665 (1998)
38 F. Schreier, J. Quant. Spectrosc. Radiat. Transf. **48**, 743 (1992)
39 B. Mayer, A. Kylling, Atmosph. Chem. Phys. **5**, 1855 (2005)
40 J. Henningsen, H. Simonsen, J. Mol. Spectrosc. **203**, 16 (2000)
41 T. Schröder, C. Lemmerz, O. Reitebuch, M. Wirth, C. Wührer, R. Treichel, Appl. Phys. B **87**, 437 (2007)
42 G. Ehret, C. Kiemle, W. Renger, G. Simmet, Appl. Opt. **32**, 4534 (1993)
43 S. Ismail, E.V. Browell, Appl. Opt. **28**, 3603 (1989)